Engineering Failure Analysis 112 (2020) 104514

Contents lists available at ScienceDirect

Engineering Failure Analysis

journal homepage: www.elsevier.com/locate/engfailanal

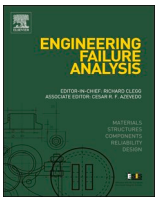

Fatigue analysis of high performance race engines

T. Rølvåg[a,*], B. Haugen[a], M. Bella[b], F. Berto[a]

[a] NTNU, Faculty of Engineering Science and Technology, 7491 Trondheim, Norway
[b] MX Research & Development Department, MXRR, 10128 Torino, Italy

ARTICLE INFO

Keywords:
Dynamic simulation
Fatigue analysis
Strain gauges
Engine simulation
FEA

ABSTRACT

This paper presents a multidiscipline dynamic simulation tool for fatigue testing. A non-linear finite element formulation embedding control system modeling is augmented to include fatigue analysis based on a mathematical representation of virtual brittle lacquer and strain rosettes. A new efficient method for rosette strain calculations based on super node displacements are applied and presented. These features are used to predict the hot spots and durability of a high performance race engine. Real physical testing is performed to capture all engine properties influencing the crank shaft stress distribution. The results predict the most critical failure modes during racing applications as well as the life in terms of drag laps before failure.

1. Introduction

Racing teams demand motorcycle engines with both high performance and structural integrity. In drag racing, the high compression engines are suffering from extreme temperatures, peak loads and high cyclical loads causing fatigue problems in pistons, bearings, connecting rods and cranks. In diesel and most street legal engines, high cycle fatigue, buckling and wear of connecting rods and pistons are common problems [1–4], but in drag racing, crank failures are more frequent according to Glenn Salpaka at Falicon Crankshaft [5].

To extend the durability of racing crankshafts Falicon uses high quality AISI 8620 steel with carburizing treatment. Plasma treatment [6], various DLC coatings [7], fillet rolling [8], shot peening [9] and material annealing [10] are other methods used to increase the crankshaft hardness and fatigue strength.

In this paper the effect of these methods can be embedded in the proposed virtual test bench developed for multidiscipline dynamic and fatigue analysis of a drag race engine [2].

A wide range of modeling and simulation tools have been developed and applied to virtual testing of engines as shown in [1,2,5,8,11–16]. This paper is based on FEDEM [17], a nonlinear FEA modeling and simulation system 18 augmented with new theory and methods for virtual fatigue testing of structural engine components subjected to dynamic loads. The methods implemented by the authors are applied on a highly customized Suzuki 1100 cc race engine performing drag laps. Virtual brittle lacquer is used to identify hot spots on the crankshaft and strain gauges are used to predict the fatigue life in terms of drag laps based on the cyclic combustion and inertia forces exerted from the piston through the connecting rod. The nonlinear FEDEM solver calculates all inertia loads, structural strains, deflections and stresses at critical engine speeds (9000–12000 rpm) during a drag lap. This objective is to demonstrate the accuracy and significant benefits of the FEDEM Test Bench (FTB) [2] for fatigue prediction of engine components like crank and connecting rods.

The paper is organized in method, fatigue theory, model, simulation and results sections. The FTB method section documents the Fedem formulations, virtual brittle lacquer and strain gauge methods for fatigue prediction. The theory section addresses the basic

* Corresponding author at: Department of Mechanical and Industrial Engineering, Norwegian University of Science and Technology (NTNU), Richard Birkelands vei 2b, 7491 Trondheim, Norway.
E-mail address: terje.rolvag@ntnu.no (T. Rølvåg).

https://doi.org/10.1016/j.engfailanal.2020.104514
Received 13 August 2019; Received in revised form 23 March 2020; Accepted 23 March 2020
Available online 24 March 2020
1350-6307/

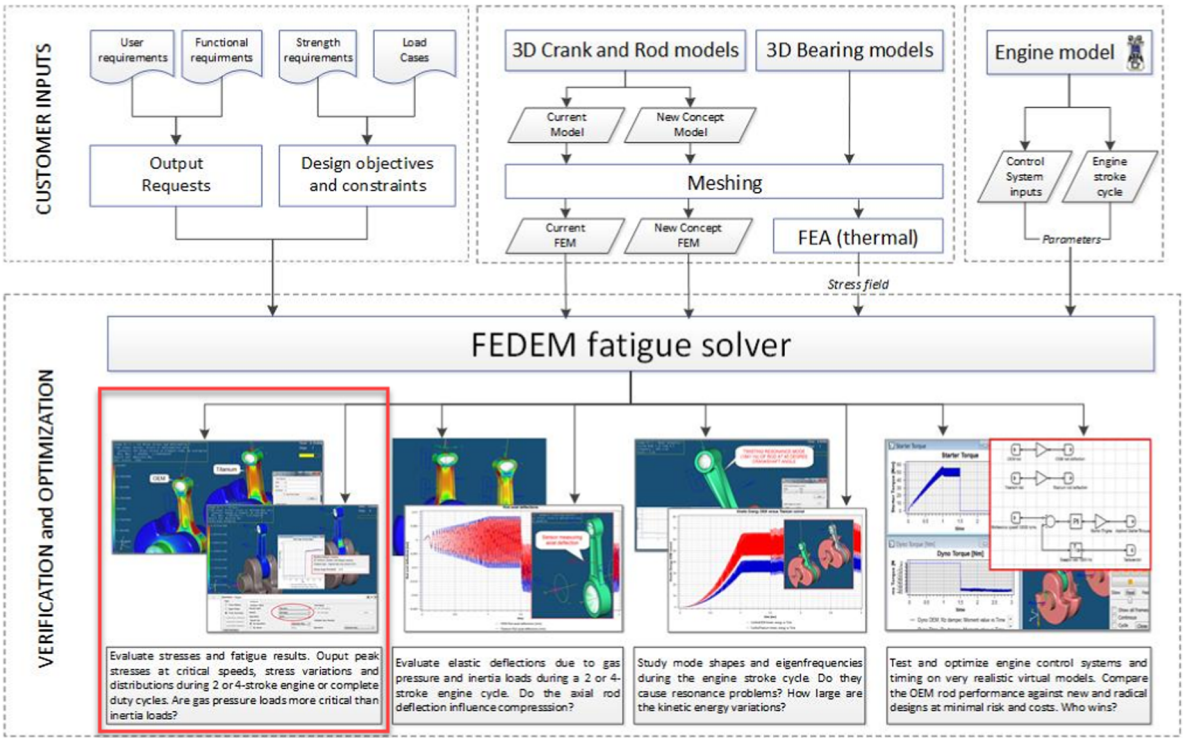

Fig. 1. The FTB augmented with fatigue features.

fatigue modeling, simulation and post processing fundamentals developed for the FTB. The model section describes the FEM components, virtual strain gages, the engine bearings, critical loads from combustion and cam shaft as well as the control and electric systems for the Suzuki drag racing engine. The simulation section demonstrates the capabilities of the FTB with respect to fatigue prediction. The results section presents the most critical crankshaft hot spots and predicted fatigue life in terms of drag laps.

2. Methods and models

2.1. The FTB multidiscipline modeling approach

Fedem is a multidisciplinary simulation system based on a non-linear finite element formulation and control system modelling and simulation. This formulation is optimized for high speed engine simulation as shown in the next section. The Fedem features/capabilities applicable to high speed engine simulations are given in [1,2,17,19]. These integrated capabilities supports a multidisciplinary modelling and simulation environment that enables the FTB to do dynamic tests and optimization of high speed engines as seen in Fig. 1.

2.2. The FTB theory

The nonlinear dynamic FEDEM solver is written on incremental form and solved by the Newmark-β time integration algorithm with respect to the displacement increments $\Delta\mathbf{r}_k$ for time increment k. To achieve equilibrium at the end of the time increment, in the non-linear case, Newton-Raphson iterations have to be used to minimize the residual forces.

$$\mathbf{M}_k\Delta\ddot{\mathbf{r}}_k + \mathbf{C}_k\Delta\dot{\mathbf{r}}_k + \mathbf{K}_k\Delta\mathbf{r}_k = \Delta\mathbf{Q}_k \tag{1}$$

where M_k, C_k, and K_k are the system mass, damping and stiffness matrices respectively at the beginning of time increment k. The system mass matrix M_k is Component Mode Synthesis (CMS) reduced and therefore always fully populated even if lumped mass representation is used for the selected finite elements. The gyro effects which has a major impact on the racing bike dynamics are therefore correctly represented. The reduced system damping matrix C_k is mass and stiffness proportional (Raleigh damping). The Raleigh damping can be used to tune low and high frequency structural damping from engine friction and oil drag. These effects can also be applied directly to the joints by using non-linear dampers and friction models. Linear and non-linear lumped masses/inertias, dampers and springs representing the flywheels, dyno brakes, piston and pins not modelled by Finite Element Models (FEMs) are directly added to the system matrices.

To achieve equilibrium at the end of the time increment, in the non-linear case, iterations have to be used to minimize the residual forces. Newton-Raphson iterations are therefore used to correct the variables (nodal displacements and modal amplitudes) towards dynamic equilibrium at the time k

$$M_k \ddot{\Delta}_k + C_k \dot{\Delta}_k + K_k \Delta_k = Q_{k+1} - [F^I_{k+1} + F^D_{k+1} + F^S_{k+1}] \quad (2)$$

where index i indicate the iteration number. Due to the high speed non-linear connecting rod behavior, the maximum number of iterations was set to 50. The system matrices M_k, C_k, and K_k were updated only the first 20 iterations (modified Newton-Raphson iterations). The minimum number of iterations was set to 2 to ensure a balance between the mechanical and control system forces. With a time step size between 1.0e−6 and 5.0e−05 s, the required number of iterations varied between 2 and 7 for a typical engine test sequence. The sequence included rewing up the engine with an electric motor to the engine power band (9000 rpm) before a drag lap is simulated with maximum engine power.

This formulation is augmented to include fast calculations of strain and stress time histories for fatigue prediction based on a CMS model reduction approach [17]. In FEDEM, each structural component is modelled as a FE superelement with a co-rotated frame for separation of elastic and rigid body displacements. The superelements are based on a component mode synthesis (CMS) method described in [17].

$$\mathbf{v}_{free} = \begin{bmatrix} \mathbf{v}_e \\ \mathbf{v}_i \end{bmatrix} = \begin{bmatrix} \mathbf{I} & 0 \\ \mathbf{B} & \Phi \end{bmatrix} \begin{bmatrix} \mathbf{v}_e \\ \mathbf{y} \end{bmatrix} = [\mathbf{H}] \begin{bmatrix} \mathbf{v}_e \\ \mathbf{y} \end{bmatrix} \quad (3)$$

where $\mathbf{v}_e$ are the external supernode displacements and y are the component mode ($\mathbf{\Phi}$) amplitudes (both updated by $\Delta\mathbf{r}_k$) contributing to the elastic displacements $\mathbf{v}_{free}$ in the condensed internal degrees of freedom $\mathbf{v}_i$ for one FE component.

2.3. Strain coat hot spot analysis

The brittle-lacquer technique of experimental stress analysis relies on the failure by cracking of a layer of a brittle coating which has been applied to the surface under investigation [18]. The coating is normally sprayed onto the surface and cracks will occur on the hot spots during physical fatigue testing. The hot spots are then indicators on where to locate strain gages for monitoring of strain/stress time histories used in fatigue analysis.

A “digital twin” of this technique that wraps a layer of “Strain Coat Elements” around each structural FEM model is developed in the FTB. One strain coat element is created for each non-interior face of the finite elements in the selected engine component. The Strain Coat Elements have no properties but acts like a distributed strain sensor applied to the surface of solid and shell elements.

When the engine loads are applied, the Strain Coat Analysis recovers the stresses and strains on all strain coat elements in the model and calculates a summary of the recovered results as it processes. The output from the strain coat analysis is a result database file for each FEM part containing the maximums of certain stress/strain quantities over the time interval considered.

Optionally, you may also perform a rainflow and fatigue analysis based on the computed stress or strain histories during the strain coat recovery. To perform rainflow and fatigue analysis during the strain coat recovery, you also need to assign an S-N curve to the selected FEM part and hence the associative “Strain Coat Elements”. The strain coat analysis will use the S-N curve in the fatigue analysis / hot spot identification.

However, the main purpose of the FTB strain coat analysis is to identify hot spots based on stress/strain quantities on the FEMs which are candidates for strain rosette locations.

2.4. Damage and life calculation

The input to the fatigue analysis is the stress/strain reading in a virtual strain gauge leg for each time step of the dynamics simulation. Alternatively one can compute the signed absolute max (ε_{samax}) principal strain from the strain rosette tensor. Letting $\{\varepsilon_1, \varepsilon_2\}$ denote the maximum and minimum principal strains which are the same as the largest and smallest eigenvalues of the symmetric strain tensor respectively, the signed absolute max value is defined through:

$$\varepsilon_{samax} = max\{|\varepsilon_1|, |\varepsilon_2|\} \quad (4)$$

Similarly, one can derive the signed absolute max principal stress, (σ_{samax}) from the stress tensor. Using Eq. (4) will normally give a more conservative life assessment compared to using a gauge leg reading, in cases where direction of the maximum strain varies during the simulated event. Using a gauge strain directly does not account for such variations.

The first step in the process of obtaining the estimated engine life at a given FEM node, is to simplify the stress/strain history curve measured by the virtual strain gauge and removing oscillations smaller than a given threshold (peak valley extraction). Fig. 2 shows the stress history reading $\sigma_{samax}(t)$ for the first 0.1 s (2.1–2.2 s) of the drag race lap, which typically consists of thousands of data points processed with a threshold of 50 MPa. In a life assessment, it is only the turning points of the curve that matter, i.e., where the gradient of the curve changes sign. Thus, after peak valley extraction using a gate value of 10 MPa, the number of data points has been reduced from 50,000 to only 30 in this case (see Fig. 2).

The next in the fatigue analysis is to perform a rainflow counting on the processed stress/strain signal, to further reduce a spectrum of varying stresses/strains into a set of simple stress/strain reversals. In the FTB algorithm [17,19], the peak and valley curve is traversed in steps looking at 3 line segments defined by four neighboring points of the curve step by step. The process is continued until the entire curve has been traversed once. The traversal is then restarted from the beginning of the curve and repeated until no full cycles could be found during one traversal. The rainflow counting outlined above can be performed in a similar manner for a stress history and a strain history curve.

Peak valley and rainflow analysis produce a list of stress ranges with magnitudes $\bar{\sigma}_i$, $i = 1. .k$, representing the entire stress history at a given node for the duration of the numerical simulation. The accumulated damage in the node can now be computed using the S-

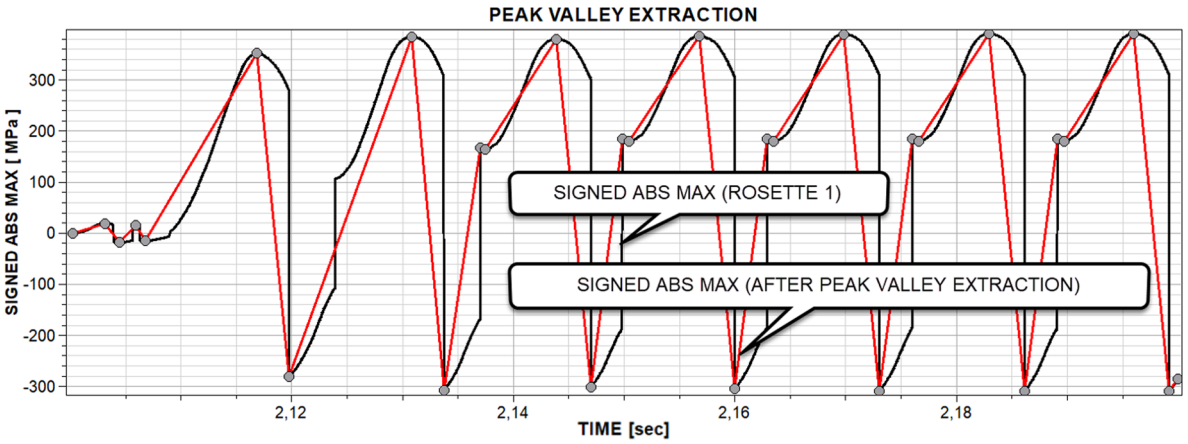

Fig. 2. The original (black) and the processed $\sigma_{samax}(t)$ (red) with threshold 50 MPa. (For interpretation of the references to colour in this figure legend, the reader is referred to the web version of this article.)

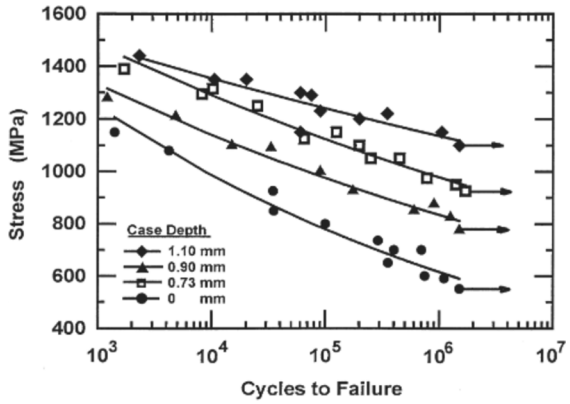

Fig. 3. Fatigue curves of heat treated and carburized AISI 8620 steel [8].

N curve for the applied engine material shown in Fig. 3. The S-N curves for the Falicon crank base material AISI 8620 is given in [20] and implemented in FEDEM based on the DNVGL RP-C203 standard [21].

According to Falicon [5], the pin and main throws have a 1 mm and a 0.25 mm carburizing treatment respectively. Only fatigue data for the base AISI 8620 material were available in [20], but FEDEM embeds S-N curves for welded steel structures as specified by DNV GL [21].

According to Radaj et al. [22], the base material steel grade has a small or no influence on the durability of welded zones. S-N curves for a DNV GL steel material was therefore used to predict the fatigue life of the crank pin welds. The welds are included in the crank FE model capturing the stress concentration, and the hotspot D-curve representing welded steel structures in air is used to calculate the fatigue life [21].

For a given set of stress ranges, $\bar{\sigma}_i$, $i = 1. .k$, the corresponding number of cycles before failure, N_1, is given from the specified S-N, curve. The accumulated damage is then computed as:

$$C = \sum_{i=1}^{k} \frac{1}{N_i} \tag{5}$$

and failure occurs when C ≥ 1.0. The estimated life in terms of number of repetitions (simulated events) is then the reciprocal of this value, 1/C. If the simulated time span is denoted T_s, the estimated life at the material node is therefore:

$$Life = \frac{T_s}{C}$$

The simulated loading event is representing one 7.5 s drag lap/pass at 10000 rpm which represents a critical load event for this engine (max compression and tension forces). FEDEM will then present the fatigue " *Life*" in seconds or number of "drag laps" before failure.

2.5. Strain rosette definitions

Four types of strain rosettes are developed. The legs are orientated by a X vector (in-plane) and a Z vector (out of plane). The Y vector (in-plane) is calculated on basis of X and Z vector. The directions are defined as shown in Fig. 4:

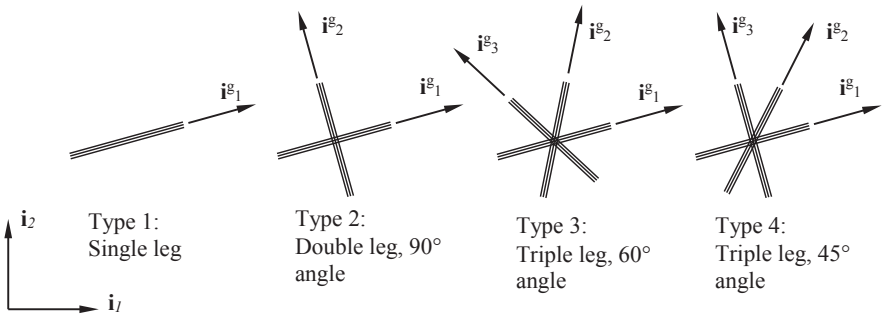

Fig. 4. Strain rosette local directions.

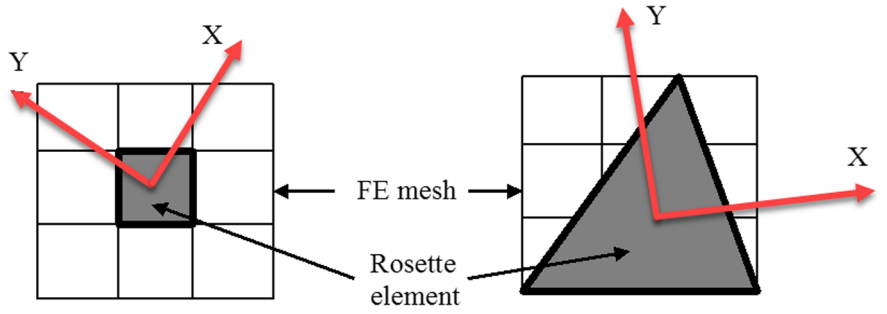

Fig. 5. The strain element is formulated as a 3 or 4 node shell element.

```
# id type link numNodes  n1  n2  n3  n4  zPos  X_x  X_y  X_z  Z_x  Z_y  Z_z  E-mod    nu
  10  2    1     4       844 846 830 828 0.0   0.0  1.0  0.0  0.0  0.0  1.0  2.06e+11 0.0
  20  4    1     3       845 846 828     0.01  0.0  1.0  0.0  0.0  0.0  1.0  2.06e+11 0.0
end
```

Fig. 6. The strain element definitions.

The basis for computing the rosette leg strains are the strains computed from a single element. Both 3 or 4 node strain measuring elements can be defined, with the strain computations at the centroid of both elements. The coordinate system in Fig. 5 represents the rosette direction defined as shown in Fig. 6.

The strain element definitions and results are presented graphically and in text files. The Cartesian strains in the rosette coordinate system, and the strains for all the legs are also printed. The material properties are by default inherited from the FE model when stress ranges are requested.

2.6. Strain rosette calculations

The rosette strains are recovered from the nodal super element displacements $\mathbf{v}_{sup}$.

$$\mathbf{v}_{free} = \begin{bmatrix} \mathbf{v}_e \\ \mathbf{v}_i \end{bmatrix} = \begin{bmatrix} \mathbf{I} & 0 \\ \mathbf{B} & \Phi \end{bmatrix} \begin{bmatrix} \mathbf{v}_e \\ \mathbf{y} \end{bmatrix} = \mathbf{H}\mathbf{v}_{sup} \tag{6}$$

Next step is to recover full FE link displacement vector from possible linear couplings:

$$\mathbf{v}_{full} = \mathbf{L}\mathbf{v}_{free} \tag{7}$$

The displacements for each strain gage element $v_{rosette}$ are extracted from v_{full}:

$$\mathbf{v}_{el} = \mathbf{A}\mathbf{v}_{full} \tag{8}$$

The rosette element displacements v_{el} are transferred to local strain gage element directions:

$$\mathbf{v}_{el} = \mathbf{T}\mathbf{v}_{el} \tag{9}$$

The strains for a strain gage element can then be expressed as:

$$\varepsilon_{el} = \mathbf{B}\mathbf{v}_{el} \tag{10}$$

The **B**matrix is the strain-displacement matrix given by the derivatives of the strain element shape functions. The strains for a strain gage element can then be transferred to the rosette coordinate system that can be chosen arbitrary by the user:

$$\varepsilon_{rosette} = \mathbf{T}_{re}\varepsilon_{el} \tag{11}$$

where $\mathbf{T}_{re}$ is the cartesian to rosette coordinate system transformation matrix. The strains in the rosette coordinate system can finally be directly related to the FE superelement DOFs $\mathbf{v}_s$:

$$\varepsilon_{rosette} = [\mathbf{T}_{re}\mathbf{BTALH}]\mathbf{v}_{sup}= \tag{12}$$

The $[\mathbf{T}_{re}\mathbf{BTALH}]$ can be precomputed for each strain gauge element which allows fast real time calculations of hot spot strains during flexible body mechanism simulations. This formulation is therefore applicable to digital twin / hardware in the loop applications.

2.7. The Suzuki engine model

The model shown in Fig. 7 is a highly customized Suzuki engine with crank and connecting rods from Falicon Crankshaft [5].

All structural engine parts are meshed with Nastran TETH10 elements and the average element size is 3 mm. The crank is instrumented with virtual strain gauges (blue markers) located on hot spots identified by the strain coat elements described in the 2.3 Strain Coat Hot Spot Analysis section.

2.8. The Suzuki combustion and inertia loads

The inertia loads at maximum speed (11000 RPM) and the combustion pressure loads at maximum torque (9000 RPM) are stretching the stress ranges causing crank fatigue problems. Based on the knowledge acquired from drag racing teams and engine builders, the authors have therefore formulated a drag lap simulation capturing both load cases:

1. An electric starter accelerates the crankshaft to 9000 rpm which is the minimum operating speed for the Suzuki engine. Maximum torque is delivered between 9000 and 10500 RPMs
2. Combustion starts and accelerates the motor to its peak performance, e.g. 182 Nm @ 10000 rpm as shown in Fig. 13. Dyno brake is activated to benchmark output torque at 10000 rpm during a 7.5 s drag lap
3. Dyno brake is turned off after 7.5 s and engine is switched off

In order to simulate the drag lap with high accuracy, the authors used a complex function to mimic the piston pressure distribution during combustion cycles. This function was first used in [2] to simulate a one-cylinder four-stroke engine but is augmented by the authors to synchronize the pressure distribution on a four-cylinder engine with a correct timing sequence. The Suzuki test results are confidential but the pressure distribution shown in Fig. 13 is representative for a 1800 cc natural aspirated engine (ATDC = 10 deg./peak pressure 11.25 MPa/peak force 70 kN @ 9000 RPM).

The pressure variation shown in Fig. 8 is controlled by the crank angle and arguments used to shape the applied Weibull functions. The engine performance (effect and torque) and hence the peak pressure is also speed dependent. Fig. 14 shows the measured torque vs. speed curve $N_3(\dot{\theta})$ for the Suzuki engine. This curve is normalized (scaled to max torque = 1) before implemented in Eq.

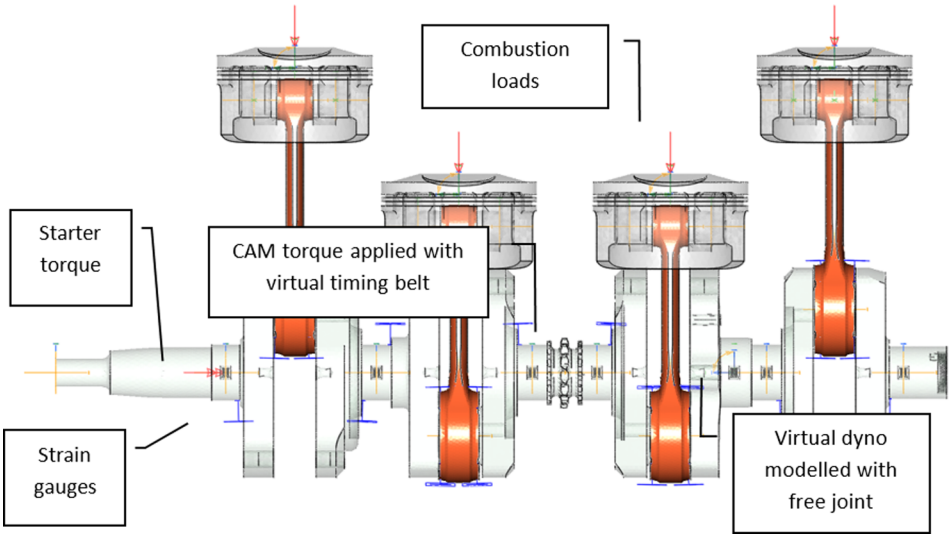

Fig. 7. Suzuki engine model.

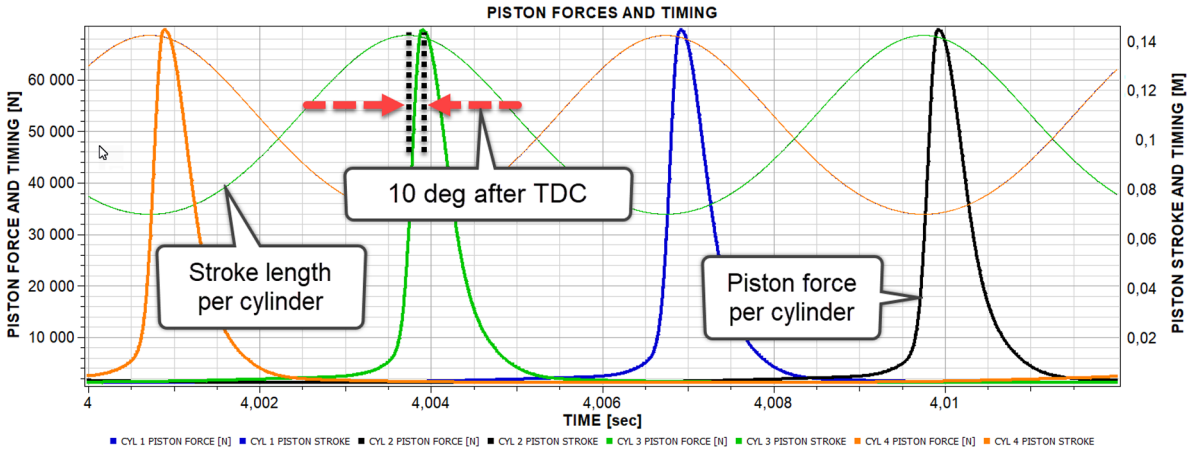

Fig. 8. Piston forces and timing.

(13) and (14). The speed dependent peak pressure for the power stroke is then given by:

$$f(\theta) = P_3\left(\left(\frac{1}{\sigma_3\sqrt{2\pi}}\right)e^{\frac{-(\theta-\mu_3)^2}{2{\sigma_3}^2}}\right)^n * N(\dot{\theta}) \quad \text{for} \quad \theta \in \langle 180° - \mu_3^\circ \rangle \tag{13}$$

$$f(\theta) = P_3\left(\frac{1}{\sigma_3\sqrt{2\pi}}\right)e^{\frac{-(\theta-\mu_3)^2}{2{\sigma_3}^2}} * N(\dot{\theta}) \quad \text{for} \quad \theta \in \langle \mu_3^\circ - 540° \rangle \tag{14}$$

where $\dot{\theta}$ is the crank shaft speed and μ_3 is the standard pressure deviation for the Weibull function describing the power stroke. Note that $P_3$is given by the compression ratio when $\dot{\theta}$ exceeds the rev. limiter speed (16000 rpm for this engine). With a compression ratio of 13.5:1 the maximum compression pressure is approx. 1.2 bar, and the combustion peak pressure is set to 11.25 MPa to give the measure maximum output torque 182 Nm @9000 RPM.

To improve the simulation speed, the measured torque curve (blue line in Fig. 9) has been estimated by a trend curve (third order polynomial) in Excel. The normalized curve is then used a speed dependent scaling factor N($\dot{\theta}$)in the Fedem user function f(θ).

To capture the crank stress variations due to the cam torques transmitted through the timing belt, physical tests were performed on a Suzuki drag race engine. The spark plugs were removed and the engine was turned at various speeds by an electric motor to measure the crank friction torque and cam axle torque due to the sharp cam profiles and valve springs. The threshold value for the peak valley extraction was set to 10 MPa to capture the stress range variations due to the measured cam axle torque.

The dynamic loads are introduced by the use of a starter engine bringing the crank to the operating speed (9000 RPMs) by a limited ramp function during 2 s as seen in Fig. 13. The reference speed function is driving the engine up to its power band 9000–12000 rpm. Then (after e.g. 2.1 sec) the engine is started by applying and syncing the piston pressure function described in the previous section. The pressure function described in the previous section is scaled with the piston area (6221 [mm^2]) to calculate the

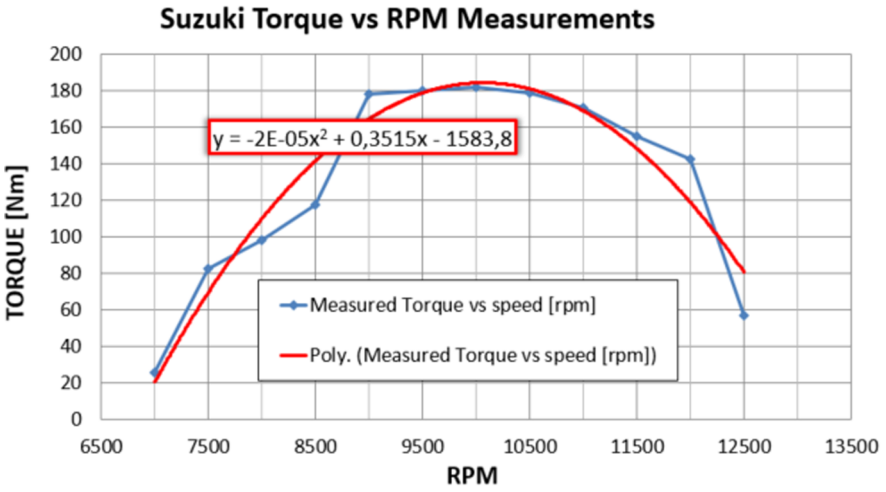

Fig. 9. Suzuki output torque vs. RPM.

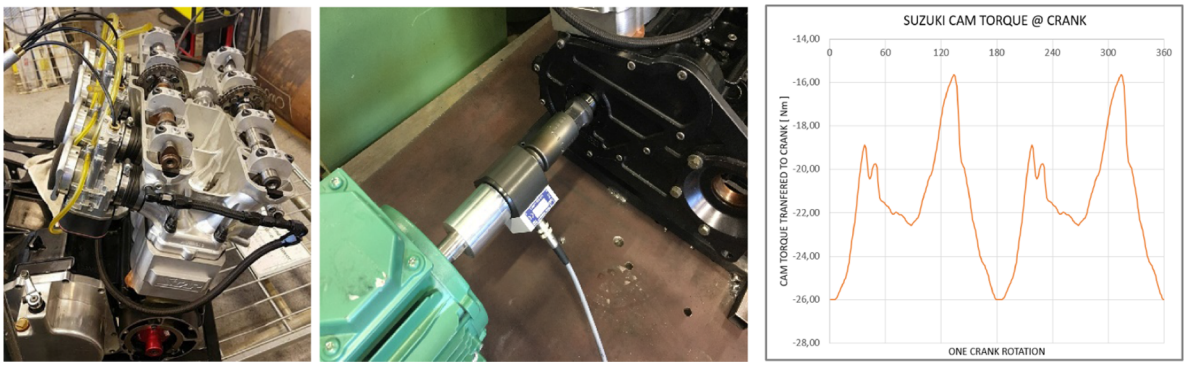

Fig. 10. Suzuki cam torque test setup and results.

applied piston force (activated by a logical switch after 2.1 s). Identical electric starter and engine control systems were modelled for all cylinders.

2.9. Cam axle torque modeling

To capture the crank stress variations due to the cam torques transmitted through the timing belt, physical tests were performed on a Suzuki drag race engine as shown for one crank rotation in Fig. 10. The spark plugs were removed and the engine was turned at various speeds by an electric motor to measure the crank friction torque and cam axle torque due to the sharp cam profiles and valve springs. The threshold value for the peak valley extraction was set to 10 MPa to capture the stress range variations due to the measured cam axle torque (see Fig. 11).

The cam torque is transmitted to the crank as indicated in Fig. 7 and Fig. 11. The torque is modelled as a joint torque versus crank angle that is modulated to vary between 0 and 360 degrees.

2.10. Engine control modeling

In the FTB, the dynamic loads are introduced by the use of a starter engine bringing the crank to the operating speed (9000 RPMs) by a limited ramp function during 2 s.

The reference speed function is driving the engine up to its power band 9000–12000 rpm. Then (after e.g. 2.1 s) the engine is started by applying and syncing the piston pressure function described in the previous section. Fig. 12 shows that the pressure function described in the previous section is connected to the input block, scaled with the piston area (6221 [mm^2]) to calculate the applied piston force (activated by a logical switch after 2.1 s). Identical electric starter and engine control systems were modelled for all cylinders.

3. Results

The Suzuki engine is accelerated until 10,000 RPM as shown in Fig. 13. At this speed, the natural aspirated Suzuki engine delivers maximum output torque 182 Nm@10000 RPM as measured by Falicon Cranks [5].

The hot spots were identified by calculating the VonMises stresses and Principal stress range magnitudes for all strain coat elements during 3 engine cycles (between 2.1 and 2.2 s) at maximum output dyno torque (182 Nm@10000 RPMs). Maximum

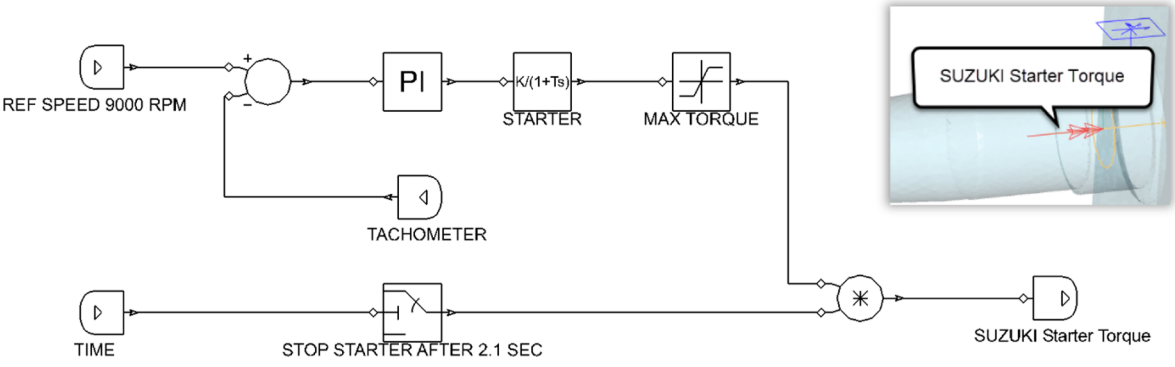

Fig. 11. The electric starter control system.

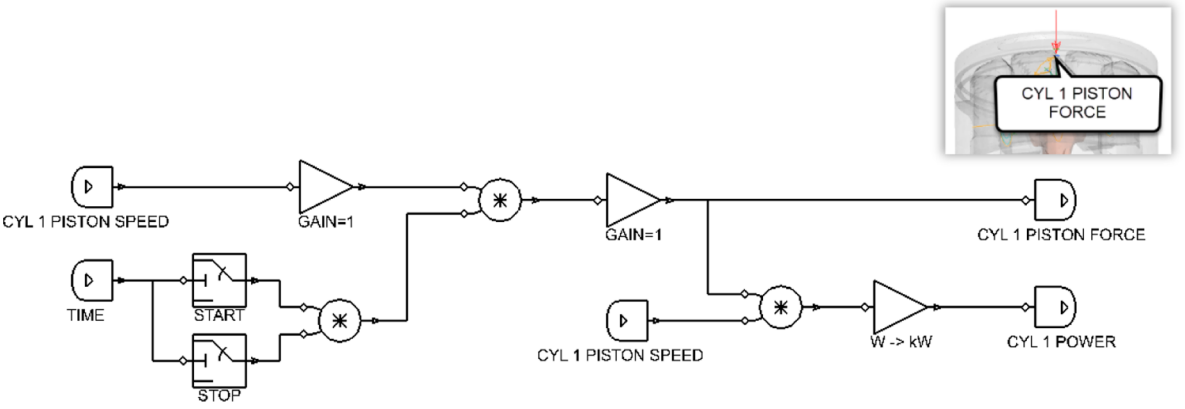

Fig. 12. Suzuki Engine Control system.

VonMises stresses in selected hot spots varied between 500 MPa 800 MPa as shown in Fig. 15.

$$\max\sigma_{VonMises} = \max_{t\in\langle 2.1-2.2\rangle} \sum_{i=1}^{n} \sigma_{i,VonMises} \tag{15}$$

The maximum Von Mises plot indicates where peak stresses occur during critical loads, but those places might not be the hot spots with maximum stress ranges. A rain flow analysis of the strain coat elements was therefore performed for the same selected engine cycles to produce the stress ranges for the crank surface. In Fig. 16, the red spots show fringe ranges above 500 MPa and the maximum calculated stress range during the selected cycles was 600 MPa. (See Fig. 17.).

$$\max\Delta\sigma = \max_{t\in\langle 2.1-2.2\rangle} \sum_{i=1}^{n} \sigma_{max} - \sigma_{min} \tag{16}$$

The identified hot spots were instrumented with 6 rosette elements (type triple gage 45, see Fig. 5). These rosettes were selected since they capture both crank bending and torsional stresses and variations in the directions of maximum principal strains/stresses. A strain rosette analysis for the complete drag lap duration 2.1–9.6 [seconds] was performed, and the strain time histories between 2.1 and 2.4 s are shown in Fig. 18. The analysis calculates strain or stress time histories as well as accumulated damage or fatigue life given as number of drag laps before failure. The signed absolute max principal stress, (σ_{samax}) range during the complete drag lap, at the selected hot spots, were between 700 and 800 MPa at 10000 rpm.

According to Falicon [5], the carburizing depth T_{ct} = 1 mm for the pin throw no 1 (cylinder 1) which gives the pin throws base material an infinite fatigue life as shown in Fig. 19. However, the fatigue life is extremely sensitive to the carburizing treatment. With a T_{ct} = 0.0 mm, the predicted fatigue life is only 89 drag laps equivalent to 11 min at strain rosette 2 as shown in Fig. 20. The fatigue life is therefore more interesting for rosette no 1 with a calculated fringe range of approx. 700 MPa in the weld zone of the main throw 1 (cylinder 1). Here, the predicted fatigue life is 5 drag laps based on the D-curve for hot spot stresses from FEA as shown in Fig. 21. A drag lap is defined as 7.5 s run at 10,000 RPMs, e.g. from 2.1 to 9.6 s simulation time as shown in Fig. 21. This is a conservative estimate since the D-curve is based on no carburizing treatment. With a T_{ct} = 1.0 mm it is reasonable to assume a fatigue life between 5 and 50 drag laps.

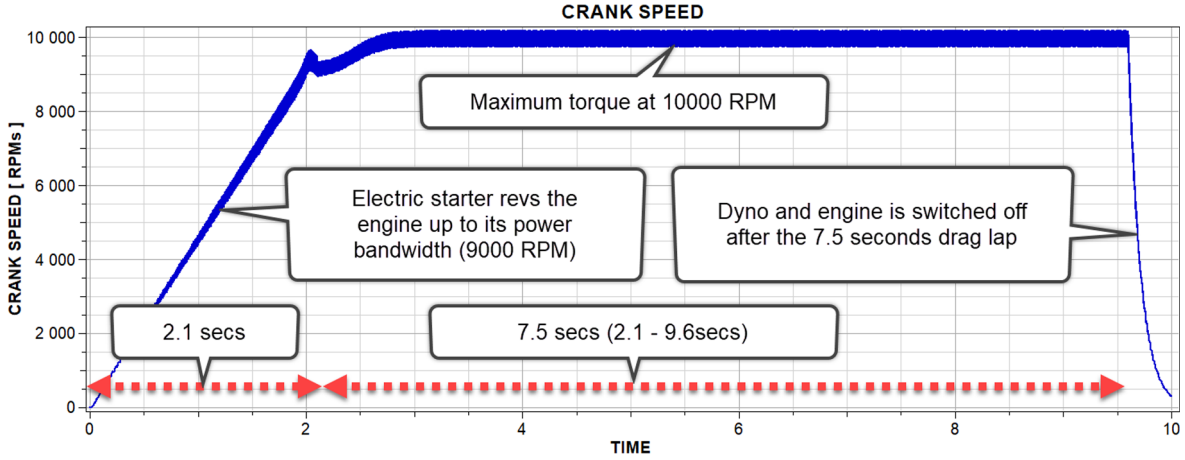

Fig. 13. Drag Lap simulation setup for maximum stress range prediction.

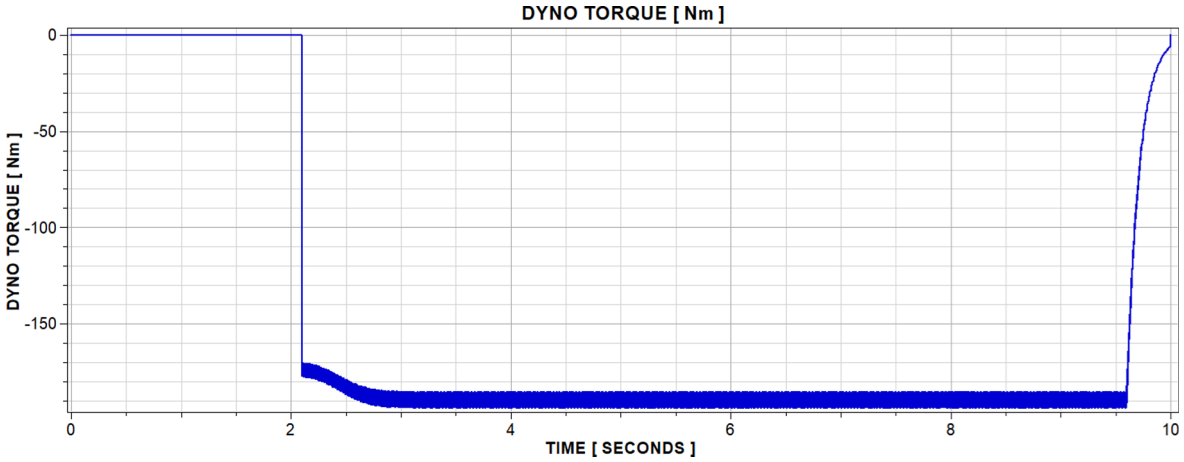

Fig. 14. Dyno output torque.

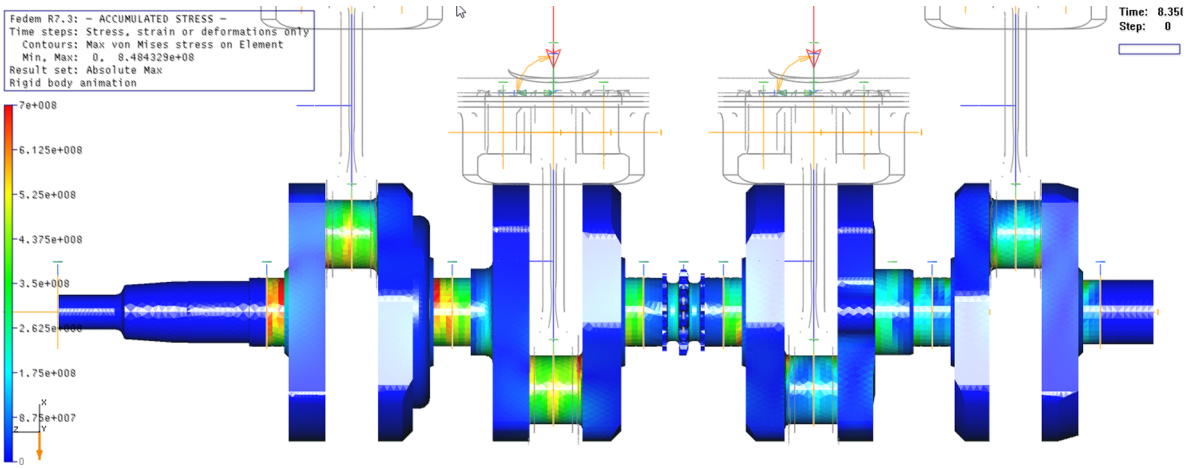

Fig. 15. Accumulated peak VonMises stresses at maximum output torque.

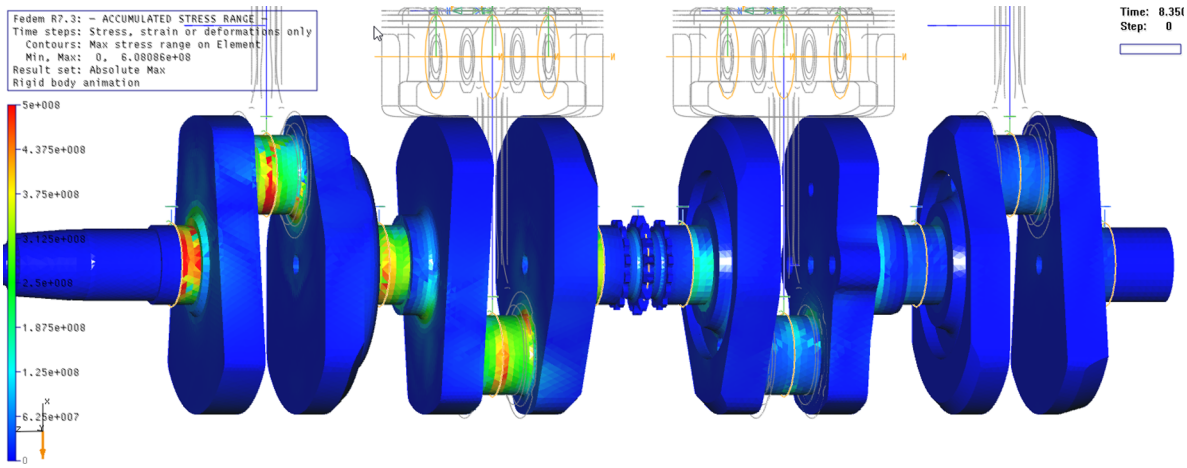

Fig. 16. Accumulated maximum stress ranges at maximum output torque.

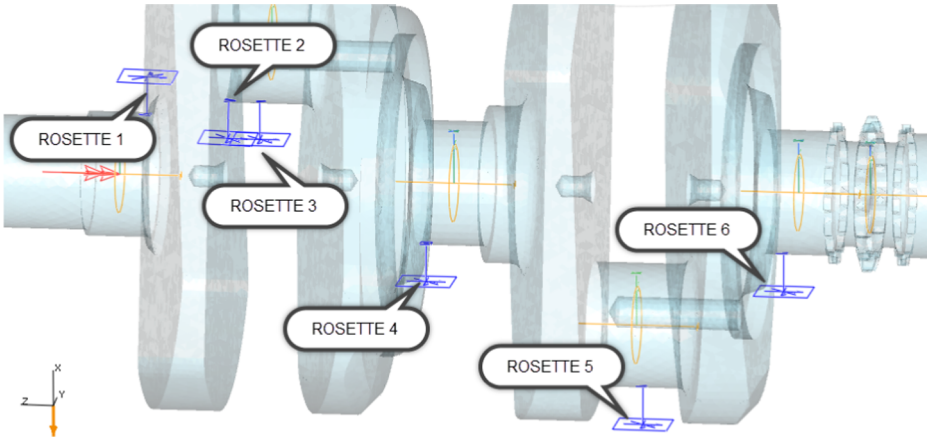

Fig. 17. Crank triple gage 45 rosettes.

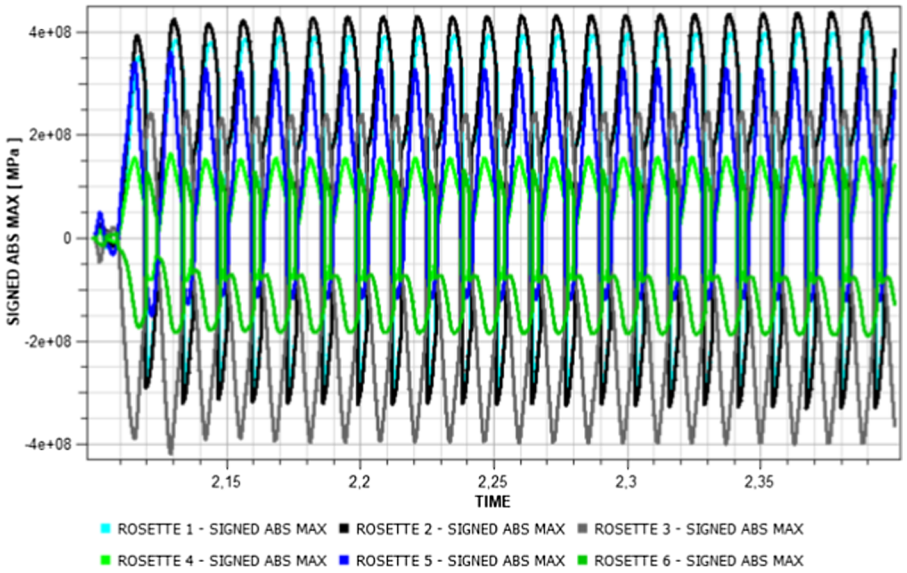

Fig. 18. Signed absolute max principal stresses.

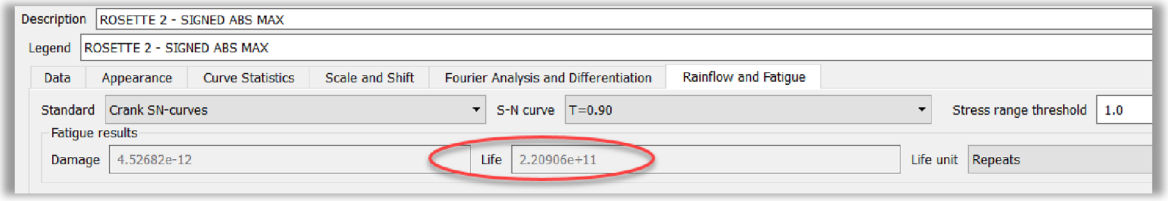

Fig. 19. Infinite fatigue life at rosette 2 with T_{ct} = 0.9 mm.

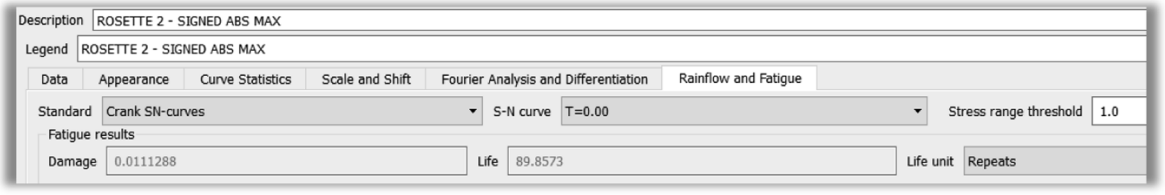

Fig. 20. Fatigue life at rosette 2 with T_{ct} = 0.0 mm.

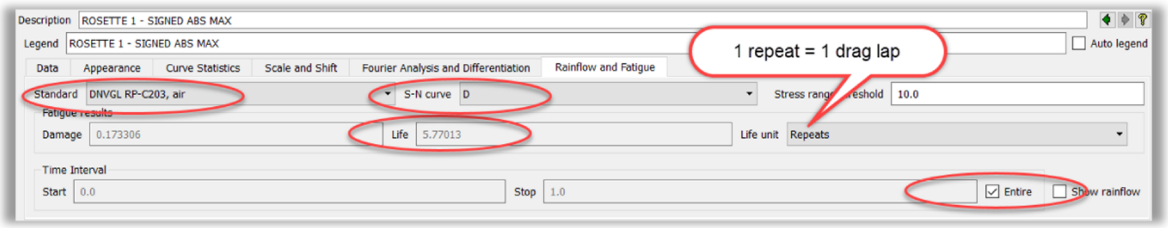

Fig. 21. Fatigue life at rosette 1 (weld zone of main throw 1).

4. Discussions

This paper presents a multidiscipline dynamic test bench (FTB) embedding multidiscipline tools for high cycle fatigue prediction of a Suzuki engine customized for drag racing.

The test bench embeds electric starters, ignition timing, power control as well as sensors and actuators enabling closed loop engine control systems. A finite element based simulation program FEDEM [1,2,17] capture dynamic engine effects which provide new knowledge about engine performance at high speeds (10000 rpm). Model reduction techniques are applied to optimize the speed and accuracy of the dynamic simulations.

These FTB features are augmented by the authors with methods for combustion load modeling and fast computations of strain time histories for various strain rosette types. An artificial brittle-lacquer technique is implemented and used to identify hotspots where strain rosettes are applied.

The strain rosette analysis outputs stress time histories used in rainflow analysis to calculate a list of stress ranges with magnitudes representing the entire stress history at a given node for the duration of the drag lap simulation. The accumulated node damage and fatigue life can be computed using the S-N curve for the applied engine material.

The predicted fatigue life is very sensitive to the weld zones and carburizing treatment having very different S-N curves. The crank base material is a high grade AISI 8620 steel with carburizing treatments between 0.25 mm (main throws) and 1 mm (pin throws). The simulation results indicate that no fatigue problems will initiate in the base material.

However, the welds do not benefit on the high grade base material and the predicted fatigue life is very short. The simulation results predict that the crank will only survive 5 drag laps before failure with no carburizing treatment. With 1 mm carburizing treatment, the crank welds will fail after 50 drag laps, which is the expected life according to Falicon Crankshaft [5].

5. Conclusion

The AISI 8620 crank base material is sensitive to the carburizing depth. A carburizing depth between 0.25 and 1 mm, gives a fatigue life prediction between 89 and infinite drag laps.

However, the welds do not benefit on the high quality base material and the predicted fatigue life is between 5 and 50 drag laps depending on the carburizing treatment.

The FTB has proven to be a robust, accurate and efficient tool for dynamic simulation. The added brittle-lacquer technique, rosette models, fast strain calculations and rainflow analysis provide an efficient digital framework for fatigue prediction of race engines. These tools can be used in high cycle fatigue prediction and to extend the durability of future race engines.

Declaration of Competing Interest

None.

Acknowledgements

The Authors would like to thank SAPECoE (former Fedem Technology AS) and Glenn Salpaka at Falicon Crankshaft Inc. for providing support and valuable inputs to the paper. We also want to thank Innovation Norway for financial support and John Deere for sharing their knowledge in fatigue software development and applications. The Virtual brittle lacquer presented in this paper was initially developed for John Deere and used to identify hot spots on their vehicles.

Appendix A. Supplementary material

Supplementary data to this article can be found online at https://doi.org/10.1016/j.engfailanal.2020.104514.

References

[1] T. Rølvåg, Using finite element modelling and simulations to test MotoGP race bikes, IJVSMT 10 (1) (2015) 74.
[2] T. Rølvåg, M. Bella, Dynamic test bench for motocross engines, Int. J. Adv. Mech. Eng. 9 (10) (2017) 1–19.

[3] S.V. Uma Maheswara Rao, T. V. Hanumanta Rao, K. Satyanarayana, B. Nagaraju, Fatigue analysis of sundry i.c engine connecting rods, Mater. Today: Proc., 5(2) Part 1 (2018) pp. 4958–4964.
[4] F.S. Silva, Fatigue on engine pistons. A compendium of case studies, Eng. Fail. Anal. 13 (3) (April 2006) 480–492.
[5] Glenn Salpaka, Falicon Crankshaft, <http://www.faliconcranks.com/>, 2018.
[6] H.J.C. Voorwald, R.G. Bonora, V.M.C.A. Oliveira, M.O.H. Cioffi, Increasing fatigue resistance of AISI 4340 steel by nitrogen plasmaion-implantation, Eng. Fail. Anal. 99 (2019) 490–499.
[7] S. Baragetti, E. Borzini, Ž. Božic, E.V. Arcier, On the fatigue strength of uncoated and DLC coated 7075–T6aluminum alloy, Eng. Fail. Anal. 99 (2019) 219–225.
[8] Gül Çevik, Rıza Gürbüz, Evaluation of fatigue performance of a fillet rolled diesel engine crankshaft, Eng. Fail. Anal. 27 (2013) 250–261.
[9] Cheng Wang, Yongbin Lai, Long Wang, Chuanli Wang, Dislocation-based study on the influences of shot peening on fatigue resistance, Surf. Coat. Technol. 38315 (2020) 125247.
[10] Sofia Papadopoulou, Ioannis Pressas, Athanasios Vazdirvanidis, George Pantazopoulos, Fatigue failure analysis of roll steel pins from a chain assembly: fracture mechanism and numerical modeling, Eng. Fail. Anal. 99 (2019) 320–328.
[11] Tadashi Niino, Tatsuya Iwamoto, Shingo Ueda, Development of simulation technology for dynamic behavior of crankshaft systems in motorcycle engines, JSAE Rev. 23 (1) (2002) 127–131.
[12] H. Saeidi Googarchin, S.M.H. Sharifi, F. Forouzesh, G.H.R. Hosseinpour, S.M. Etesami, S. Malek Zade, Comparative study on the fatigue criteria for the prediction of failure in engine structure, Eng. Fail. Anal. 79 (2017) 714–725.
[13] M. Fonte, P. Duarte, V. Anes, M. Freitas, L. Reis, On the assessment of fatigue life of marine diesel engine crankshafts, Eng. Fail. Anal. 56 (2015) 51–57.
[14] Xiao-lei Xu, Zhi-wei Yu, Bing Yu, Fatigue failure of an intermediate transition block in fuel-injection pump fork assembly of a truck diesel engine, Eng. Fail. Anal. 94 (2018) 13–23.
[15] Yury M. Temis, Mathematical simulation of low cycle fatigue of high-loaded engine parts, Propul. Power Res. 7 (4) (2018) 277–287.
[16] Darko Pastorcic, Goran Vukelic, Zeljko Bozic, Coil spring failure and fatigue analysis, Eng. Fail. Anal. 99 (2019) 310–318.
[17] Ole Ivar Sivertsen, Virtual Testing of Mechanical Systems, Swets & Zeitlinger, Lisse, 2001.
[18] E.J. Hearn et al., Experimental Stress Analysis, Mechanics of Materials 1 (Third Edition), 1997.
[19] Knut M. Okstad et al., Fedem Release 7.3 Theory Guide, 2019.
[20] Kenan Genela, Mehmet Demirkol, Effect of case depth on fatigue performance of AISI 8620carburized steel, Int. J. Fatigue 21 (1999) 207–212.
[21] DNVGL RP-C203 standard, 2019, <https://rules.dnvgl.com/docs/pdf/DNVGL/RP/2016-04/DNVGL-RP-C203.pdf>.
[22] Dieter Radaj, C.M. Sonsino, W. Fricke, Fatigue Assessment of Welded Joints by Local Approaches, ISBN: 9781845691882, 2006.